How to cite: *Angew. Chem. Int. Ed.* **2023**, *62*, e202303129
doi.org/10.1002/anie.202303129

Covalent Organic Frameworks | Hot Paper

Tuning Local Charge Distribution in Multicomponent Covalent Organic Frameworks for Dramatically Enhanced Photocatalytic Uranium Extraction

Hui Yang, Mengjie Hao, Yinghui Xie, Xiaolu Liu, Yanfang Liu, Zhongshan Chen, Xiangke Wang,* Geoffrey I. N. Waterhouse, and Shengqian Ma**

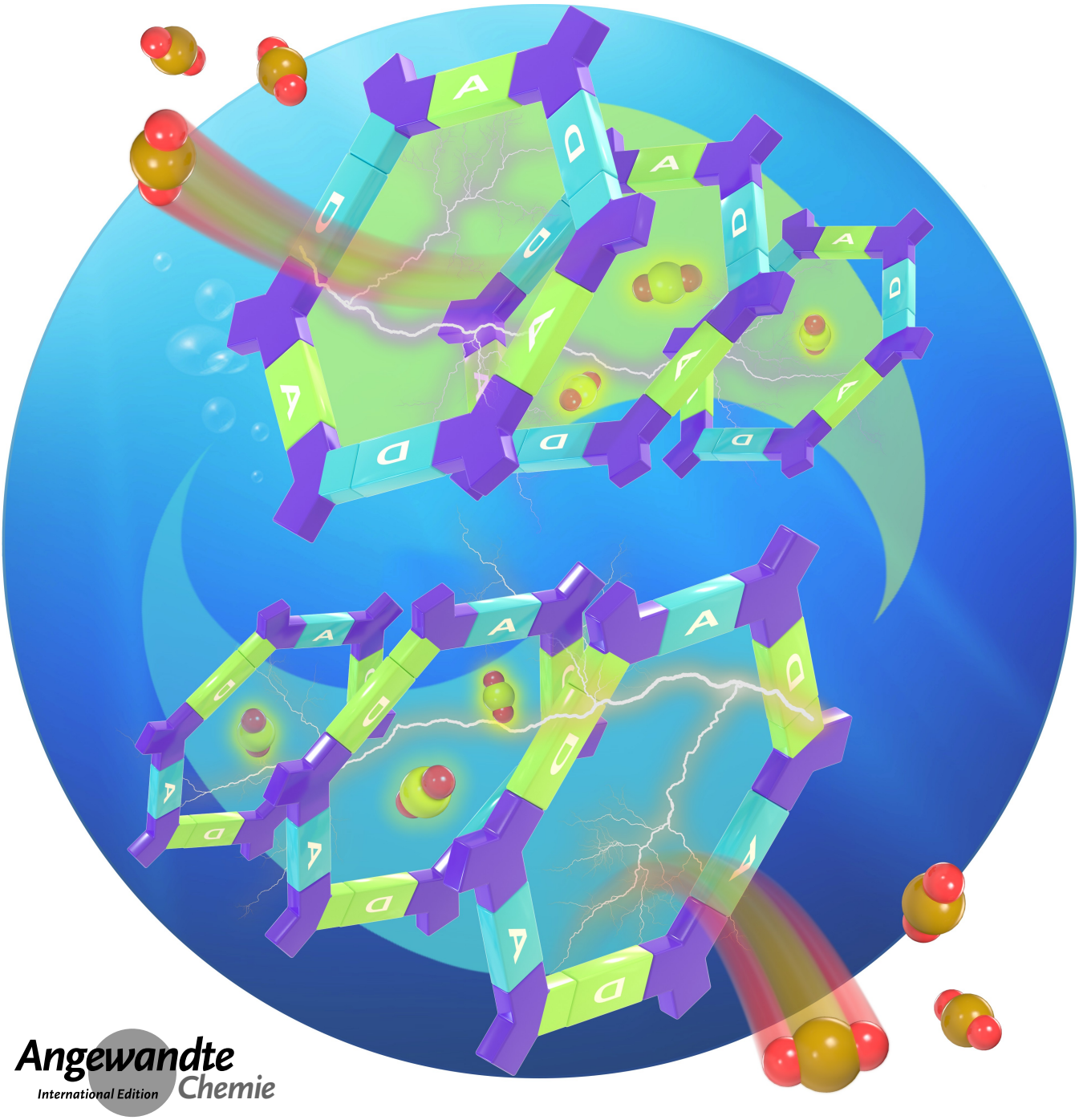

Abstract: Optimizing the electronic structure of covalent organic framework (COF) photocatalysts is essential for maximizing photocatalytic activity. Herein, we report an isoreticular family of multivariate COFs containing chromenoquinoline rings in the COF structure and electron-donating or withdrawing groups in the pores. Intramolecular donor-acceptor (D-A) interactions in the COFs allowed tuning of local charge distributions and charge carrier separation under visible light irradiation, resulting in enhanced photocatalytic performance. By optimizing the optoelectronic properties of the COFs, a photocatalytic uranium extraction efficiency of 8.02 mg/g/day was achieved using a nitro-functionalized multicomponent COF in natural seawater, exceeding the performance of all COFs reported to date. Results demonstrate an effective design strategy towards high-activity COF photocatalysts with intramolecular D-A structures not easily accessible using traditional synthetic approaches.

Introduction

Due to their compositional flexibility and tunable pore characteristics, covalent organic frameworks (COFs)[1] are gaining importance in energy storage and conversion,[2] sensing,[3] separation,[4] environmental remediation,[5] and catalysis.[6] The functionality of COFs depends on the linkers or building blocks used in their construction and their spatial arrangement. In this context, introducing functional groups on the organic linkers is an effective way to tune the pore characteristics of COFs. Cooperatively combining two or more different functional groups into COF pores can engender beneficial synergistic functions.[7] This has motivated researchers to construct multicomponent COFs with emergent properties not found in typical single- or two-component frameworks.[8]

Recently, COFs have attracted attention as photocatalysts,[9] due to their well-defined pores,[10] suitable electronic band gap,[11] efficient exciton migration,[12] rapid photogenerated charge separation and transfer kinetics,[13] and long charge carrier lifetimes.[14] In many studies, cobaloxime co-catalysts were used to improve photocatalytic efficiency and stability of COFs.[15] Chen and co-workers showed that halogen modulation of COF linkers could efficiently suppress charge recombination and significantly reduce the energy barrier for visible-light-driven hydrogen evolution.[16] Subsequently, a series of isoreticular COFs were prepared to explore the main factors influencing visible-light-driven photocatalytic H_2 production.[17] Next, porphyrinic covalent organic frameworks were synthesized, with the incorporation of Zn^{2+} and Ni^{2+} cations found to regulate excitonic effects, greatly improving photocatalytic performance.[18] In recent notable contributions, several research groups have built donor-acceptor (D-A) systems to enable effective photogenerated charge separation and efficient charge migration.[19] These findings have opened up new avenues for the design of efficient COF-based photocatalysts. In these works, D-A systems were created by preparing electron-deficient or electron-donating linkers separately, then self-assembling the linkers into COFs with D-A heterojunctions (Figure 1a). In these systems, the donor and the acceptor linkers are often connected by imine bonds[19] which hinders electron transport properties, representing a significant bottleneck in the development of high-performance COF photocatalysts. For such COFs, there is a lack of fundamental understanding of the relationship between the internal electronic structure of the COFs and the factors affecting catalytic activity at a molecular level.

Isoreticular chemistry allows the design and synthesis of functional COFs for specific applications.[1a,7,20] Inspired by this guiding chemistry principle, we herein propose a general strategy for the design of multivariate COFs incorporating tunable photocatalytic components, in which electron exciton behaviors and photocatalytic activity were modulated by tuning the local charge distribution in pores. The donor and acceptor sites of COFs were rationally tuned by introducing the electron donating and attracting groups on the linkers, resulting in different local charge distributions (Figure 1b). To achieve this objective, we first designed and synthesized a family of tertiary COFs through molecular engineering concepts (Figure 1c). In a subsequent step, post-synthetic modification transformed propenyloxy groups to chemically stable chromenoquinoline rings through the Povarov reaction, eliminating imine bonds and increasing π-conjugation, thereby creating novel donor-acceptor systems and COFs with greatly enhanced photocatalytic activity (Figure 1c). We then systematically explored the relationships between the pore characteristics and photocatalytic properties of the COFs under visible light irradiation, using uranium extraction from seawater as a test reaction. The analysis revealed that a number of the post-synthetically modified COFs fabricated in this work (COF 4P, COF 6P, and COF 7P) were particularly efficient photocatalysts for uranium extraction in the absence of any sacrificial reagents. COF 4P delivered fast kinetics and a high uranium uptake efficiency of 8.02 mg/g/day in natural seawater, a record-high extraction efficiency for a COF-based material. An array of experimental methods and theoretical calculations revealed that the electron attracting (electron-withdrawing ability follows: nitro > bromine > pyridine N) and donating groups (electron-donating ability follows: o-dihydroxy ≈ p-dihydroxyl > methoxyl) anchored on the aromatic rings of

[*] H. Yang, M. Hao, Y. Xie, X. Liu, Y. Liu, Z. Chen, X. Wang
College of Environmental Science and Engineering, North China Electric Power University
Beijing 102206 (P.R. China)
E-mail: h.yang@ncepu.edu.cn
xkwang@ncepu.edu.cn
G. I. N. Waterhouse
School of Chemical Sciences, The University of Auckland
Auckland 1142 (New Zealand)
S. Ma
Department of Chemistry, University of North Texas
Denton, TX-76201 (USA)
E-mail: shengqian.ma@unt.edu

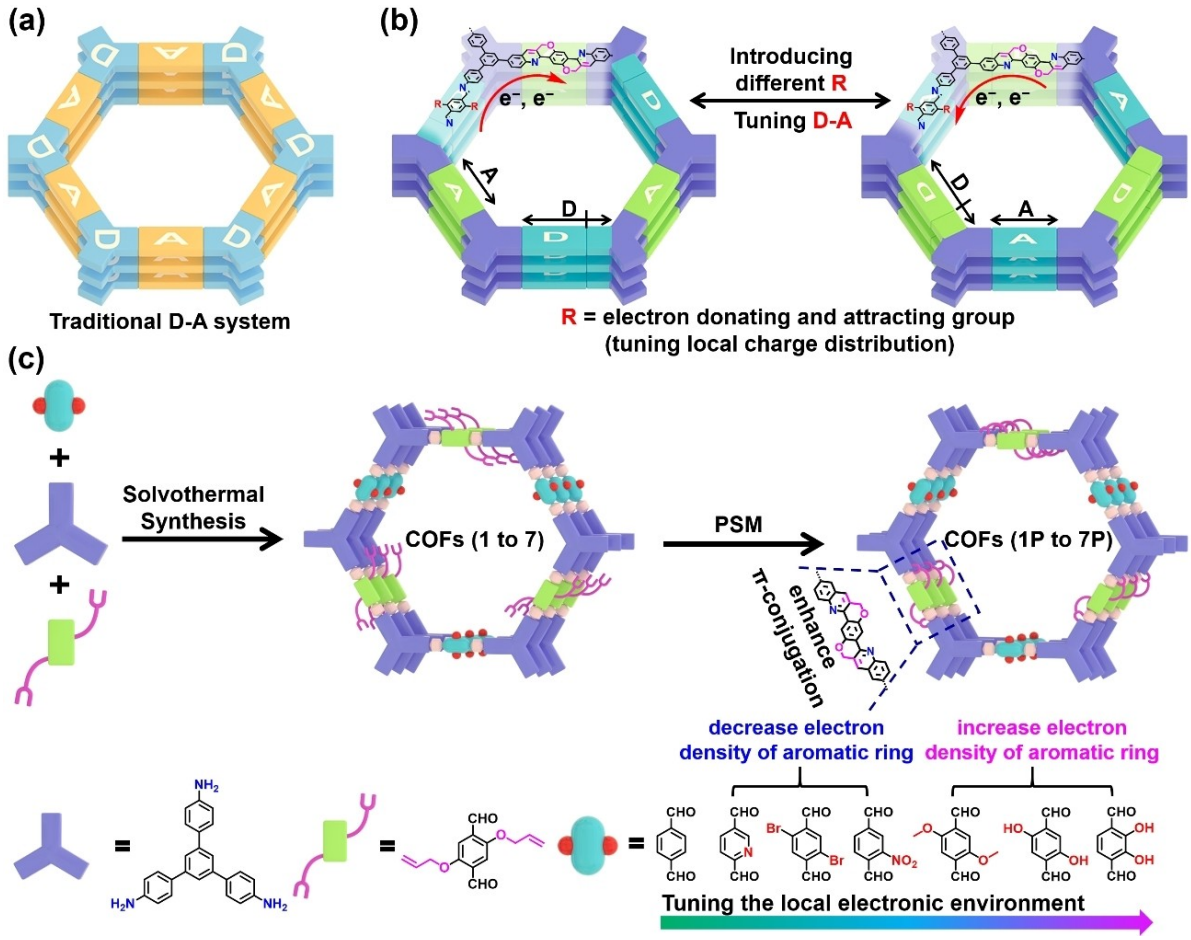

Figure 1. a) Schematic illustration of a traditional donor-acceptor (D-A) system in COF photocatalysts. b) Schematic illustration of our strategy for the construction of D-A systems through introducing electron donating and attracting groups on aromatic linkers in multivariate COF photocatalysts. c) Illustration of the synthesis of COFs 1P to 7P, highlighting that the local electronic environment can be programmed by a combination of post-synthetic modification strategy and installation of remote linkers.

the linkers in the COFs created a non-uniform distribution of electron clouds on the aromatic rings, effectively enhancing the intramolecular interactions between electron donors and acceptors in the pores, thus improving the optoelectronic properties of the COFs and improving charge carrier separation. In comparison, aromatic ring linkers with uniformly distributed electron clouds demonstrated poor photocatalytic activities due to the overlapped locally excited states, thus decreasing intramolecular interactions between donors and acceptors. Importantly, the multicomponent nature of these frameworks allowed us to understand and optimize the factors influencing photocatalytic performance, guiding the future design of improved COF-based photocatalysts for different applications.

Results and Discussion

Quinoline-based COFs demonstrate photothermal conversion ability under visible light irradiation.[21] Accordingly, we hypothesized that the incorporation of chromenoquinoline rings into multivariate COF frameworks might be beneficial for enhancing photocatalysis. Figure 1c shows that general synthetic route adopted in this work for the preparation of COFs, which was amenable to the incorporation of a variety of substituents onto the multivariate framework and late-stage conversion of the propenyloxy groups to quinoline rings. In the first stage, isoreticular tertiary COFs (denoted as COF 1 to COF 7) were synthesized via an imine condensation of 1,3,5-tris(4-aminophenyl)benzene, 2,5-bis-(allyloxy)terephthalaldehyde, and 1,4-phthalaldehyde analogues with acetic acid as the catalyst in a mixture of mesitylene/1,4-dioxane at 120 °C for 3 days. Subsequently, post-synthetic conversion of synthesized imine COFs to chromenoquinoline-based COFs (denoted as COFs 1P to 7P, respectively) were achieved through Povarov reactions under solvothermal conditions.[21b]

Fourier transform infrared (FT-IR) spectra for COFs 1 to 7 (Figures 2a, S1) showed the disappearance of the characteristic NH_2 and C=O signals at ≈3340 cm^{-1} and 1685 cm^{-1}, respectively, of the linkers, together with the appearance of new peaks at ≈1613 cm^{-1} and ≈1588 cm^{-1} associated with imine C=N stretching vibrations. After the post-synthetic reaction, the C=N stretching vibrations (

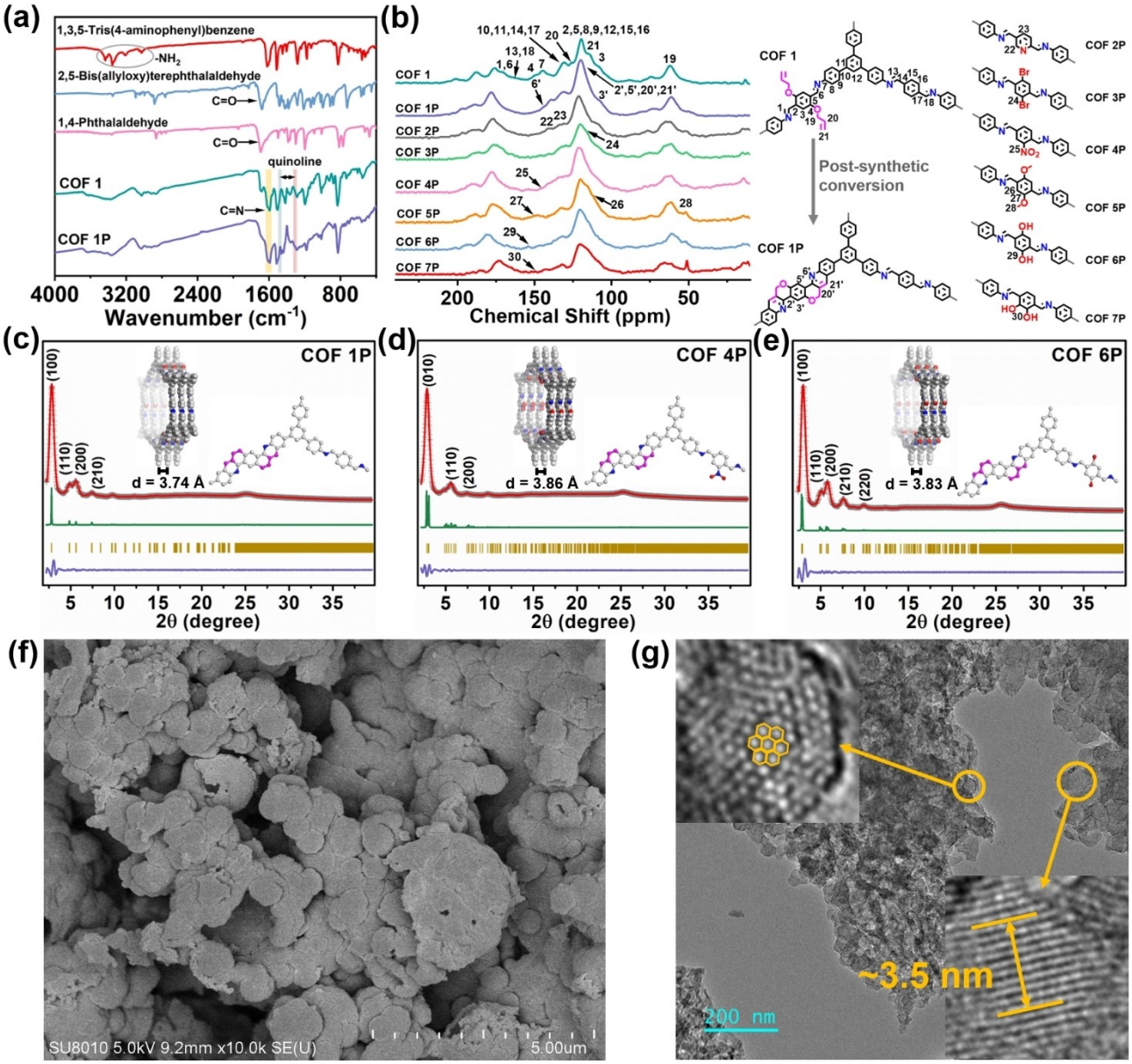

Figure 2. a) FT-IR transmittance spectra for COFs 1, 1P, and linkers. b) ^{13}C CP-MAS solid-state NMR spectra of COFs 1, 1P, 2P, 3P, 4P, 5P, 6P, and 7P. c), d), e) Experimental PXRD patterns of COFs 1P, 4P, and 6P with corresponding Pawley refinement (red), simulated results (green), and Bragg positions (khaki) showing good fit to the experimental data (gray) with minimal differences (dark violet). The inset shows the structural models of each COF assuming the eclipsed (AA) stacking mode. f) SEM image of COF 4P. g) HRTEM image of COF 4P (insets highlight the honeycomb-like pores).

$\approx$1613 cm^{-1} and $\approx$1588 cm^{-1}) were retained, with new signals being observed at 1461 cm^{-1} and 1313 cm^{-1}, demonstrating the success formation of the chromenoquinoline rings in COF 1P to COF 7P.[21b,22] The solid-state ^{13}C cross-polarization with magic-angle spinning (CP-MAS) NMR spectrum of COF 1 showed signals at 62, 126, and 114 ppm due to vinyl carbon atoms on the propenyloxy groups, whilst the aromatic carbon atoms gave peaks at 131 and 119 ppm (Figure 2b). Subsequently, the solid-state ^{13}C NMR spectra of COFs 1P to 7P showed the disappearance of vinyl carbon signals at 114 and 126 ppm, further confirming the formation of chromenoquinoline rings (Figure 2b). The post-synthetically modified COFs could be "fingerprinted" on the basis of carbon signals associated with specific functional groups in the 1,4-phthalaldehyde analogue-derived linkers in each COF: COF 2P (pyridine ring, 141 and 134 ppm), COF 3P (carbon bonded to bromine, 116 ppm), COF 4P (carbon bonded to a nitro group, 146 ppm), COF 5P (methoxyl group and carbon bonded to methoxyl group, 151, 111, 52 ppm), COF 6P (carbon bonded to a hydroxyl, 154 ppm), and COF 7P (carbon bonded to a hydroxyl group, 149 ppm).

Powder X-ray diffraction (PXRD) and Pawley refinement analysis were employed to study the crystallinity of the newly constructed COFs (COFs 1, and 1P to 7P). All the

PXRD patterns revealed microcrystalline materials (Figures 2c–e, S2, S3, Tables S1–S8). Similar to COF 1 (Figures 2c, S2), the diffraction pattern of COF 1P showed intense peaks at $2\theta \approx 2.8°$, 4.9°, 5.6°, and 7.4°, which were assigned to the 100, 110, 200, and 210 reflections of π–π stacked two dimensional (2D) crystalline layers. The experimental results agreed well with a simulated pattern for an eclipsed (AA) stacking mode constructed using Material Studio software (Figure 2c). The evidence from Pawley fitting refined unit cell parameters revealed that COF 1P crystalized in a triclinic *P*1 space group with unit cell parameters of $a = 36.78$ Å, $b = 36.73$ Å, $c = 3.74$ Å, $\alpha = 97.67°$, $\beta = 96.92°$, and $\gamma = 118.67°$ with $R_P = 2.96\,\%$, $R_{wp} = 4.24\,\%$ (Table S2). Results confirmed COF 1P possessed hexagonal pores with an estimated pore size of 3.61 nm (Figure S4). The interlayer distance was approximately 3.74 Å (Figure 2c). The crystalline structures of COFs 2P to 7P were also determined using experimental PXRD data, structure modelling, and Pawley refinements (Figures 2d, e, S3–S10, Tables S3–S8). The results showed that all these COFs exhibited similar reflections and unit cell parameters to COF 1P, indicating all possessed isostructural porous neutral frameworks. Scanning electron microscopy (SEM) images showed COFs 1P to 7P to consist of aggregated microspheres (Figures 2f, S11). High-resolution transmission electron microscopy (HRTEM) revealed that the individual microspheres were composed of smaller nanosheets (Figures 2g, S12). HRTEM also allowed the internal structures of the COFs to be probed. One-dimensional channels were observed for COFs 1P to 7P, revealing the ordered alignment with high degrees of crystallinity, consistent with the porous structures measured by PXRD analysis (Figures 2g, S12).

The porosity of COFs 1P to 7P were determined by nitrogen sorption isotherms on fully activated samples at 77 K. All samples displayed type-IV adsorption/desorption isotherms, indicating the presence of mesoporous structures (Figure 3a). The calculated Brunauer–Emmett–Teller (BET) surface areas of COF 1P, COF 2P, COF 3P, COF 4P, COF 5P, COF 6P, and COF 7P were 862.4, 775.5, 1129.3, 655.4, 690.8, 773.7, and 301.1 $m^2 g^{-1}$, respectively. Density functional theory (DFT) analysis revealed the average pore size in the COFs ranged from ≈3.3 nm to ≈3.8 nm, in good accord with the predicted pore diameters for the eclipsed AA geometries (Figure S13). These results suggest that the high order within the lattices of the COFs contributes to their large porosity, which was expected to facilitate efficient mass transport during photocatalysis. The thermal stabilities of COFs 1P to 7P were evaluated by thermogravimetric

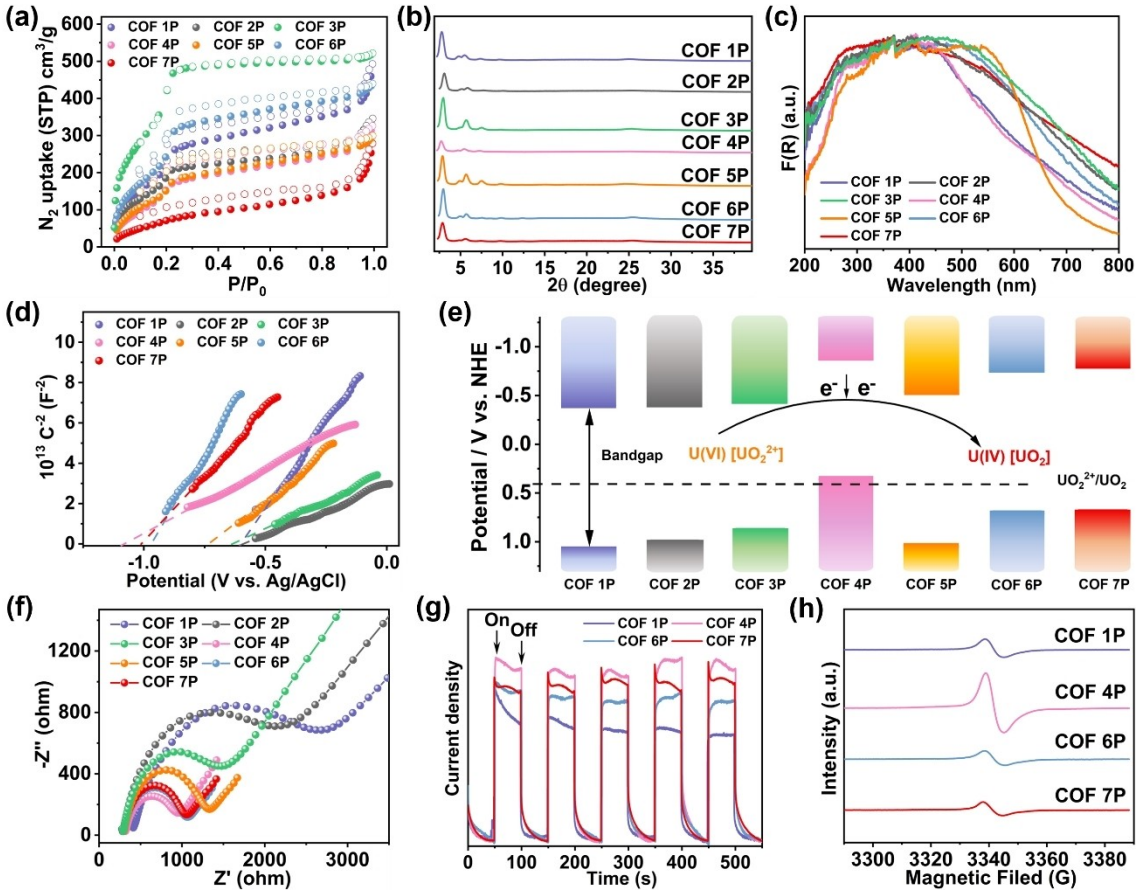

Figure 3. a) N_2 sorption isotherms measured at 77 K for COFs 1P to 7P. b) PXRD patterns for COFs 1P to 7P after treatment in natural seawater. c) UV-visible diffuse reflectance spectra for each COF. d) Mott–Schottky plots for each COF. e) Band alignment of each COF. f) EIS spectra of each COF. g) Photocurrent responses of each COF. h) EPR conduction band e-signals of each COF.

analysis (TGA) under a N_2 atmosphere. The TGA curves revealed that these COFs were thermally stable up to ≈330 °C (Figure S14). Next, we carried out chemical stability tests on the COFs by immersing the powder samples in natural seawater, HNO_3 (3 M), and NaOH (3 M) solutions. After 3 days, the powder samples were collected and characterized by PXRD. Negligible changes in the characteristic PXRD peaks were found after these treatments, indicating the COFs possessed excellent chemical stability (Figures 3b, S15, S16). The robust structure and chemical properties of the COF samples suggested suitability for photocatalytic applications under high ionic strength conditions.

UV/Visible diffuse reflectance spectroscopy (UV/Vis DRS), electrochemical impedance (EIS), transient photocurrent, and electron paramagnetic resonance (EPR) spectroscopy were performed to systematically investigate the photophysical and electrochemical properties of COFs 1P to 7P. All COFs absorbed strongly between 200 to 800 nm (Figure 3c), indicating good visible-light-harvesting ability. The optical band gap energies determined from the Kubelka–Munk function transformed spectra were 1.48, 1.42, 1.34, 1.25, 1.59, 1.48 and 1.51 eV for COFs 1P, 2P, 3P, 4P, 5P, 6P, and 7P, respectively (Figure S17). These narrow band gap energies suggest that the COF photocatalysts should offer good visible-light-driven photocatalytic activities. COFs 1 to 7 showed relatively narrow light absorption bands (Figure S18). Next, Mott–Schottky tests were carried out to estimate the valence and conduction band positions in the COFs. The obtained Mott–Schottky plots (C^{-2} vs E) for the COFs showed a positive slope typical of n-type semiconductors, with flat band values (E_{fb}, vs *Ag/AgCl*) of −0.60, −0.61, −0.65, −1.09, −0.74, −0.97, and −1.01 V for COFs 1P, 2P, 3P, 4P, 5P, 6P, and 7P, respectively (Figure 3d). This data together with the band gap data allowed the valence band (VB) and conduction band (CB) edges of the COFs to be calculated (Figure 3e). Subsequently, the electronic conductivity of the COFs were studied by EIS. COFs 4P, 6P, and 7P exhibited a smaller semicircle in the Nyquist plots, indicating a lower charge transfer resistance and more efficient charge carrier transport and separation compared to the other COFs (Figure 3f). Subsequently, photocurrent measurements were conducted to evaluate the photoelectric responses of COFs 1P, 4P, 6P, and 7P (Figure 3g). Anodic photocurrents were detected under chopped light (on/off) irradiation for all the COFs. The light responses of COF 4P, COF 6P, and COF 7P were higher than COF 1P, suggesting excellent charge separation ability and stability under light irradiation. Light-induced charge carrier generation in the COFs was also verified using EPR spectroscopy. COF 1P, COF 4P, COF 6P, and COF 7P exhibited signals around g = 2.004, indicating the formation of the conduction band electrons under visible light excitation (Figure 3h). Among the COFs, COF 4P showed the strongest signal, indicating better charge carrier generation efficiency. Taken together, these results suggest that the developed COFs could be utilized as an effective photocatalyst platform for uranium extraction from seawater due to their well-defined structures, high porosity, good visible-light-harvesting ability, negative E_{fb} positions, and excellent charge separation and transport properties, which satisfy the requirement for U^{VI} reduction to U^{IV} [0.411 V vs. *normal hydrogen electrode (NHE)*].[23] As proof-of-concept, we next conducted a series of photocatalytic experiments to assess the viability of the COFs for uranium extraction from seawater. In particular, we aimed to explore the effect of the local electron donating and attracting functional groups on the framework linkers on the photocatalytic performance.

Nuclear power generated by fission reactors using enriched uranium (^{235}U) fuel has a very low carbon footprint, and thus is expected to play an important role in achieving carbon neutrality by 2050.[25] However, uranium ore reserves on land are limited, motivating researchers to pursue uranium extraction from seawater (where the amount of uranium is ≈1000 times higher than on land, albeit highly dispersed as dissolved uranyl ions).[26] Adsorption-based technologies developed to date for uranium extraction from seawater are not economically viable due to the low uranium concentration in seawater (≈3.3 ppb) together with the large amounts of other competing metal ions, high salinity, and marine biofouling.[24,27] Therefore, significant improvements in the uranium extraction efficiency from seawater are needed to meet practical requirements. The COF photocatalysts reported herein provided the opportunity identify the key factors needed for the selective and efficient photocatalytic reduction of U^{VI} to a U^{IV} solid product (UO_2), allowing valuable structure-photocatalytic activity relationships to be established. We first evaluated the photocatalytic performance of the COF photocatalysts in ≈20 ppm uranium spiked seawater. The experiments were carried out under visible light without using any sacrificial reagents. As expected, COF 4P demonstrated the fastest uranium extraction kinetics among all COFs, delivering an adsorption capacity of 449.3 mg/g U after 8 h (Figure 4a). COFs 6P and 7P showed slightly lower extraction efficiencies (354.7 mg/g for COF 6P and 396.1 mg/g COF 7P, respectively). By comparison, the U^{VI} removal capacities of COF 2P, COF 3P, and COF 5P were only 281.7 mg/g, 291.8 mg/g, and 328.1 mg/g, respectively, though these were all higher than COF 1P which displayed slow kinetics and poor U uptake. Notably, COF 4P possessed extremely rapid uranium extraction abilities in a ≈90 ppb spiked seawater sample, with removal ratios of 92.9 % and 99.6 % within 1 h and 3 h, respectively (Figure 4b). Stability is vital property for photocatalysts. Thus, we performed durability tests on COF 4P using cycles of uranium extraction under similar conditions. Negligible changes in uranium uptake were found after five cycles, with PXRD and FT-IR results showing the used COF retained its original structure. Results confirmed COF 4P possessed outstanding stability (Figures S19–S21). In addition, after the uranium adsorption tests, the presence of an uranium oxide species was detected by the FT-IR spectroscopy and uranium by energy dispersive spectroscopy (Figures S20, S22). SEM showed the original morphology of COF 4P was retained after photocatalysis (Figure S22). Notably, all chromenoquinoline functionalized COFs showed much higher U^{VI} removal ratios than their parent COFs, indicating the photocatalytic activity of the COFs was improved through the intramolecular cycloaddition post-synthetic modification (Figure S23).

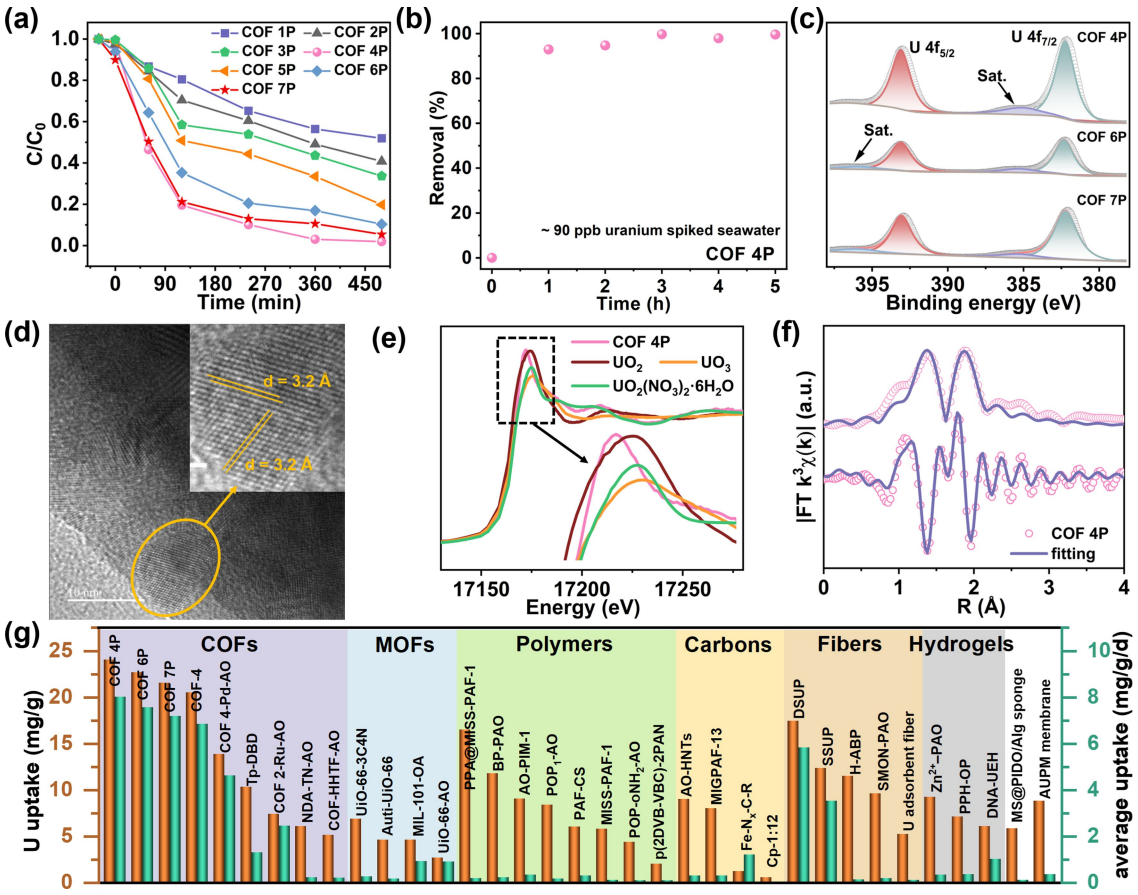

Figure 4. a) Uranium extraction from spiked seawater with initial uranium concentrations of ≈20 ppm, using COFs (1P to 7P) as photocatalysts. b) Uranium extraction from spiked seawater with initial uranium concentrations of ≈90 ppb, using COF 4P as photocatalyst. c) XPS spectra of COFs 4P, 6P, and 7P after photocatalysis. d) HRTEM image of COF 4P after photocatalysis. e), f) XANES and EXAFS spectra of COF 4P after photocatalysis. g) Comparison of uranium extraction uptake performance of COFs 4P, 6P, 7P and other reported materials in natural seawater. The reference data for UO_2, UO_3, and $UO_2(NO_3)_2{\cdot}6H_2O$ in 4e were taken from our previous work.[24]

The generated U^{IV} solid product was identified to be UO_2, based on X-ray photoelectron spectroscopy (XPS), U L_3-edge X-ray absorption fine structure (XAFS), and HRTEM results. The U 4f XPS spectra of COFs 4P, 6P, and 7P after photocatalysis showed peaks at 382.3 and 393.1 eV in a 4:3 area ratio, which could readily be assigned to the $4f_{7/2}$ and $4f_{5/2}$ signals, respectively, of a U^{IV} species (Figure 4c). The formation of UO_2 was definitively confirmed by the HRTEM image of an attached solid nanoparticle (Figure 4d). Lattice fringes with a d-space of ≈3.2 Å were observed, which could be readily indexed to the (111) planes of a cubic UO_2. The U L_3-edge X-ray absorption near-edge structure (XANES) spectrum of COF 4P after photocatalysis was similar to that of the UO_2 standard, with the edge position being typical for U^{IV}, consistent with the XPS results (Figure 4e). The Fourier transformed extended XAFS (EXAFS) spectrum exhibited main peaks at 1.4 Å and 1.9 Å, corresponding to the first U–O and second coordination shells in UO_2, respectively (Figure 4f, Table S9). Moreover, peak fitting indicated that each U atom was coordinated by approximately seven O atoms, typical for UO_2 (Figure S24).

Since COFs 4P, 6P, and 7P demonstrated excellent photocatalytic activities for U^{VI} reduction, we then evaluated their uranium extraction ability in natural seawater. Uranium uptake with time was recorded under visible light irradiation. All three COFs demonstrated fast uptakes with uranium extraction capacities of 24.1, 22.7, and 21.6 mg/g achieved for COF 4P, COF 6P, and COF 7P, respectively, after 3 days (Figure 4g). To the best of our knowledge, COF 4P showed the highest uranium extraction capacity ever reported for a COF, with record-high extraction efficiency (8.02 mg/g/day) in natural seawater. This value exceeds the all other COF photocatalysts and adsorbents reported thus far (Figure 4g). A comprehensive comparison of different COF-based materials for uranium extraction is provided in Table S10. In addition, we studied the selectivity of COF 4P for U^{VI} uptake over other metal ions in natural seawater, including Zn^{II}, Cr^{III}, Fe^{III}, Ni^{II}, Cu^{II}, and V^{V} (Figure S25). The selectivity of COF 4P towards uranium was several-fold higher than the other metal ions. Importantly, the selectivity towards uranium was about five times higher than that towards vanadium during the photocatalytic processing, suggesting good potential applicability in uranium extraction from seawater. Since COF 4P demonstrated

excellent photocatalytic U^{VI} reduction performance, we conducted an economic feasibility analysis. Our calculations estimated the cost of synthesizing COF 4P to be ≈4.7 USD/g, suggesting economic feasibility of the photocatalyst for practical applications.

Biofouling is a serious problem for most adsorbents, seriously affecting the efficiency of uranium extraction from seawater. Biofouling can passivate active sites and also prevent light from reaching the photocatalysts, thereby compromising the activity of the photocatalysts. Accordingly, we evaluated the anti-biofouling properties of COFs 1P, 4P, 6P, and 7P by testing their inhibition of marine bacteria (mixture), *Synechococcus elongatus* (*S. elongatus*), and *Chlorella sorokiniana* (*C. sorokiniana*) before and after visible light irradiation. These bacteria and algae are abundant in the ocean and play an important role in marine biofouling. The results are summarized in Figures 5a–d, S26, and Table S11. COF 4P showed 23.57 %, 28.45 %, and 45.42 % inhibition of the marine bacteria, algae *S. elongatus*, and *C. sorokiniana*, respectively, under dark conditions. Under visible light irradiation, the anti-biofouling activity of COF 4P increased dramatically, resulting in high inhibition rates of 96.78 %, 59.67 %, 81.34 % for marine bacteria, algae *S. elongatus*, and *C. sorokiniana*, respectively. COFs 6P and 7P showed similar activities to COF 4P with high inhibition rates of 93.55 % and 95.12 % towards marine bacteria under visible light conditions. Moreover, COFs 6P and 7P offered high inhibition rates against *S. elongatus*, and *C. sorokiniana* (Table S11). In comparison, COF 1P showed lower antimicrobial ability under the same testing conditions.

It is widely understood that superoxide radicals ($^{\bullet}O_2^-$), singlet oxygen ($^1O_2$), and hydroxyl radicals ($^{\bullet}OH$) produced by photocatalysts under visible light irradiation can damage the cell walls of marine microorganisms.[27a] EPR studies were thus carried out to identify the radicals generated in the photocatalytic process by COFs 1P, 4P, 6P, and 7P in the dark and under visible light irradiation (Figures 5e, f, S27). No EPR signals was detected under dark conditions for any of the COFs. Conversely, under light irradiation, $^{\bullet}O_2^-$ and $^{\bullet}OH$ were generated and trapped using 3,4-dihydro-2,3-dimethyl-2*H*-pyrrole 1-oxide (DMPO), whilst $^1O_2$ was also detected after adding 2,2,6,6-tetramethylpiperidine (TEMP) as the trapping agent. The evolution of these reactive oxygen species explained the excellent anti-biofouling activity of the COFs under light irradiation. Taken together, the photogenerated electrons in the COFs reduced U^{VI} to U^{IV}, whilst the oxygen-containing radicals formed through the interaction of O_2 with the COF suppressed the growth of marine microbes, thus ensuring efficiently uranium extraction photocatalysis in seawater (Figure 5g).

To gain deep insights into the selective photocatalytic U^{VI} extraction mechanism, we carried out time-resolved photo-

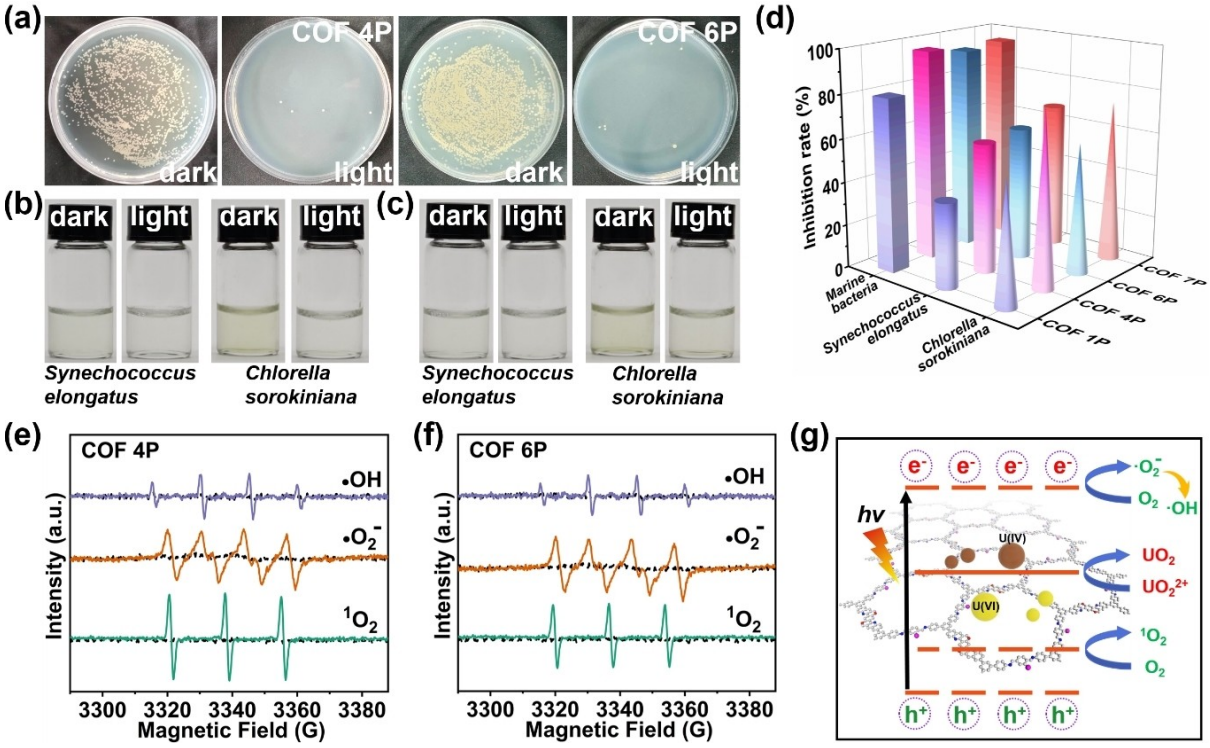

Figure 5. a) Photographs of marine bacteria after treatment with COF 4P (left) and COF 6P (right) in the dark and under visible light conditions. b) Photographs of *Synechococcus elongatus* (*S. elongatus*) and *Chlorella sorokiniana* (*C. sorokiniana*) treated with COF 4P under dark and visible light conditions. c) Photographs of *S. elongatus* and *C. sorokiniana* treated with COF 6P under dark and visible light conditions. d) Summary of anti-biofouling activity of COFs 1P, 4P, 6P, and 7P under visible light conditions. e), f) EPR spectra for $^{\bullet}O_2^-$-DMPO, $^{\bullet}$OH-DMPO, and $^1O_2$-TEMP complexes formed under visible light irradiation of COFs 4P and 6P. The black spectra were collected from samples kept in the dark, the colored curved for samples exposed to visible light. g) Proposed photocatalytic mechanism used by the COFs.

luminescence emission decay spectroscopy (TRPL) and transient absorption spectroscopy (TAS) measurements on the COFs to evaluate their photogenerated charge carrier utilization efficiency. The TRPL spectra showed that the average fluorescence lifetimes of COF 4P (0.96 ns) and COF 7P (0.59 ns) were significantly longer than those of COF 1P (0.39 ns) and COF 6P (0.42 ns). The longer lifetime indicates that the rate of recombination of photogenerated charge carriers was lower in COF 4P and COF 7P (Figures 6a, S28). Subsequently, the charge transfer dynamics in COF 4P was studied by TAS, which also probes the lifetime of the photogenerated charges. A 450 nm pulsed laser was used as the excitation source. As shown in Figure 6b, the spectra for COF 4P showed broad negative bleaching signals in the range of 650–950 nm. The negative bleaching signals are associated with the generation of excited electrons. Fitting the TAS kinetic plots allowed determination of the lifetime of charge carriers in COF 4P, which showed a long lifetime of 80.7 ns (Figure 6c). These results verified COF 4P possessed slow electron-hole combination kinetics, explaining the highly active photocatalytic for U^{VI} reduction. The data also revealed that the charge carrier utilization efficiency of these COFs followed the order COF 4P > COF 7P ≈ COF 6P > COF 1P. Since the COFs differed only in their structural components on the 1,4-phthalaldehyde-derived linkers, results suggested structure–activity relationships played an important role in regulating the photocatalytic activity. In particular, the presence of nitro and hydroxyl groups in the pores of the functionalized COFs appeared to greatly enhance the photocatalytic performance.

To better understand the structure-photocatalytic performance relationship, electrostatic potential (ESP) distribution analysis were performed for COFs 1P, 4P, and 6P. As shown in Figures 6d–f, the ESP distribution of COF 1P was comparatively homogeneous. However, the introduction of the strongly electron-attracting nitro group (in COF 4P) or strongly electron-donating hydroxyl groups (in COF 6P) enhanced the local polarization of the framework in comparison to COF 1P, which appeared to be a key factor contributing to their enhanced photocatalytic activities. Next, we carried out natural transition orbitals (NTOs) analysis to identify the electron-hole distribution in the COFs using time-dependent density functional theory (TDDFT) calculations. As displayed in Figure 6e, when strongly electron-attracting nitro groups were attached to the 1,4-phthalaldehyde-derived linker (COF 4P), the excited state hole was distributed on both the 1,3,5-triphenylben-

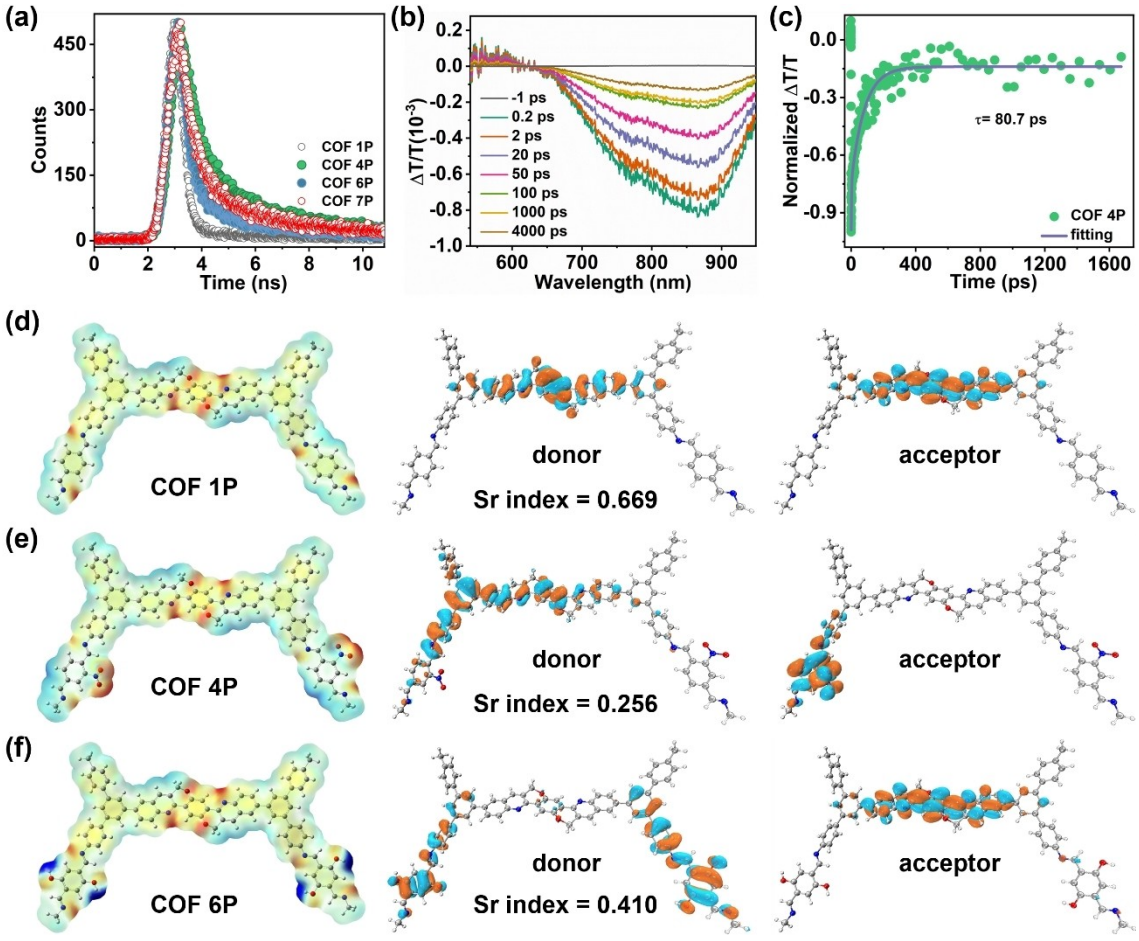

Figure 6. a) Time-resolved photoluminescence (TRPL) spectra of COFs 1P, 4P, 6P, and 7P (excitation at 375 nm) (b) Time slices of the transient absorption spectra (TAS) for COF 4P (at λ_{ex} = 450 nm). c) TAS and fitting curves of COF 4P (at λ_{ex} = 450 nm). d), e), f) The electrostatic potential, donor, and acceptor distributions for COFs 1P, 4P, and 6P.

zene and chromenoquinoline ring, while the excited electron was mainly located on the 2-nitroterephthalaldehyde component, which served as the electron transport site. However, the donor and acceptor sites were located within the hexagonal ring (pore) when hydroxyl was attached to the 1,4-phthalaldehyde-derived linker (as in COF 6P). Accordingly, the chromenoquinoline rings acted as sites for photo-induced electron accumulation, whereas parts of the C_3 linker together with phenol components served sites of electron depletion in COF 6P (Figure 6f). In comparison, the electron and hole distribution overlapped the chromenoquinoline sites in the absence of extra functional groups (COF 1P), which prevented efficient electron transport from the electron donor to the U^{VI} acceptor (Figure 6d).

Taking the above experimental and theoretical calculations into account, the results demonstrate that the linker components strongly influence photo-induced electron-hole separation in the multivariate COF photocatalysts and also excited charge transfer between donor and acceptor. The presence of electron-donating groups or electron-withdrawing groups can tune the local electric charges, in a way that is beneficial for electron-hole pair separation and efficient charge carrier utilization, resulting in enhanced photoreduction activity toward uranium extraction from seawater. Photocatalytic activity increased with electron-attracting groups in the order $-NO_2 > -Br >$-pyridine N, and with electron-donating groups in the order $-OH > -OCH_3$. Other factors that enhanced the photocatalytic of the isoreticular COFs described herein (especially COF 4P) were the structural regularity and crystallinity of the COFs, excellent visible light harvesting ability, efficient photogenerated charge separation, and transfer kinetics. Further, the high porosity of the COFs allowed efficient mass transport and fast charge carrier transfer, resulting in efficient uranium extraction from seawater with potent anti-biofouling properties under visible light.

Conclusion

In summary, we have designed and successfully synthesized a family of isoreticular 2D multicomponent COF photocatalysts via systematic engineering of the building blocks at a molecular level. The experimental and theoretical studies verified that post-synthetic generated chromenoquinoline rings enhanced the π-conjugation of the framework, and the local polarization generated through organic linker modification (by adding electron withdrawing or donating groups) tuned the charge separation and utilization efficiency, creating novel intramolecular donor-acceptor (D-A) systems. One of our developed COFs, COF 4P, possessed an extremely high uranium uptake capacity of 8.02 mg/g/day under visible light, state-of-the-art performance for any COF-based adsorbent or adsorbent-photocatalyst in natural seawater. Our work lays a platform for the design of improved COF-based photocatalysts for uranium extraction from seawater and other applications.

Acknowledgements

We gratefully acknowledge funding support from the National Key Research and Development Program of China (2018YFC1900105), National Science Foundation of China (Grants U2167218; 22006036; 22276054), the Beijing Outstanding Young Scientist Program (HY, ZC, and XW), and the Robert A. Welch Foundation (B-0027) (SM). GINW is supported by a James Cook Research Fellowship from New Zealand Government funding, administered by the Royal Society Te Apārangi. We also acknowledge support from the 14W station in Shanghai Synchrotron Radiation Facility (SSRF).

Conflict of Interest

The authors declare no conflict of interest.

Data Availability Statement

The data that support the findings of this study are available from the corresponding author upon reasonable request.

Keywords: Charge Distribution · Covalent Organic Frameworks · Donor-Acceptor · Photocatalysis · Post-Synthesis

[1] a) S. J. Lyle, P. J. Waller, O. M. Yaghi, *Trends Chem.* **2019**, *1*, 172–184; b) A. M. Evans, L. R. Parent, N. C. Flanders, R. P. Bisbey, E. Vitaku, M. S. Kirschner, R. D. Schaller, L. X. Chen, N. C. Gianneschi, W. R. Dichtel, *Science* **2018**, *361*, 52–57; c) R. Liu, K. T. Tan, Y. Gong, Y. Chen, Z. Li, S. Xie, T. He, Z. Lu, H. Yang, D. Jiang, *Chem. Soc. Rev.* **2021**, *50*, 120–242.

[2] a) X. Zhao, P. Pachfule, A. Thomas, *Chem. Soc. Rev.* **2021**, *50*, 6871–6913; b) Y. Yusran, Q. Fang, V. Valtchev, *Adv. Mater.* **2020**, *32*, 2002038.

[3] W. K. Haug, E. M. Moscarello, E. R. Wolfson, P. L. McGrier, *Chem. Soc. Rev.* **2020**, *49*, 839–864.

[4] Z. Wang, S. Zhang, Y. Chen, Z. Zhang, S. Ma, *Chem. Soc. Rev.* **2020**, *49*, 708–735.

[5] X. Liu, H. Pang, X. Liu, Q. Li, N. Zhang, L. Mao, M. Qiu, B. Hu, H. Yang, X. Wang, *The Innovation* **2021**, *2*, 100076.

[6] Y. Zhi, Z. Wang, H. L. Zhang, Q. Zhang, *Small* **2020**, *16*, 2001070.

[7] B. Zhang, H. Mao, R. Matheu, J. A. Reimer, S. A. Alshmimri, S. Alshihri, O. M. Yaghi, *J. Am. Chem. Soc.* **2019**, *141*, 11420–11424.

[8] a) L. Chen, K. Furukawa, J. Gao, A. Nagai, T. Nakamura, Y. Dong, D. Jiang, *J. Am. Chem. Soc.* **2014**, *136*, 9806–9809; b) S. Tao, H. Xu, Q. Xu, Y. Hijikata, Q. Jiang, S. Irle, D. Jiang, *J. Am. Chem. Soc.* **2021**, *143*, 8970–8975; c) A. Jati, K. Dey, M. Nurhuda, M. A. Addicoat, R. Banerjee, B. Maji, *J. Am. Chem. Soc.* **2022**, *144*, 7822–7833; d) Z. F. Pang, S. Q. Xu, T. Y. Zhou, R. R. Liang, T. G. Zhan, X. Zhao, *J. Am. Chem. Soc.* **2016**, *138*, 4710–4713.

[9] a) G.-B. Wang, K.-H. Xie, H.-P. Xu, Y.-J. Wang, F. Zhao, Y. Geng, Y.-B. Dong, *Coord. Chem. Rev.* **2022**, *472*, 214774; b) H. Wang, H. Wang, Z. Wang, L. Tang, G. Zeng, P. Xu, M. Chen, T. Xiong, C. Zhou, X. Li, D. Huang, Y. Zhu, Z. Wang, J. Tang, *Chem. Soc. Rev.* **2020**, *49*, 4135–4165; c) S. Bi, Z. Zhang, F. Meng, D. Wu, J. S. Chen, F. Zhang, *Angew. Chem. Int. Ed.*

2022, *61*, e202111627; d) S. Bi, F. Meng, D. Wu, F. Zhang, *J. Am. Chem. Soc.* **2022**, *144*, 3653–3659.
[10] a) M. Traxler, S. Gisbertz, P. Pachfule, J. Schmidt, J. Roeser, S. Reischauer, J. Rabeah, B. Pieber, A. Thomas, *Angew. Chem. Int. Ed.* **2022**, *61*, e202117738; b) S. Zhang, G. Cheng, L. Guo, N. Wang, B. Tan, S. Jin, *Angew. Chem. Int. Ed.* **2020**, *59*, 6007–6014; c) F. Auras, L. Ascherl, A. H. Hakimioun, J. T. Margraf, F. C. Hanusch, S. Reuter, D. Bessinger, M. Doblinger, C. Hettstedt, K. Karaghiosoff, S. Herbert, P. Knochel, T. Clark, T. Bein, *J. Am. Chem. Soc.* **2016**, *138*, 16703–16710; d) Z. B. Zhou, P. J. Tian, J. Yao, Y. Lu, Q. Y. Qi, X. Zhao, *Nat. Commun.* **2022**, *13*, 2180.
[11] W. K. Han, Y. Liu, X. Yan, Y. Jiang, J. Zhang, Z. G. Gu, *Angew. Chem. Int. Ed.* **2022**, *61*, e202208791.
[12] a) X. Zhang, K. Geng, D. Jiang, G. D. Scholes, *J. Am. Chem. Soc.* **2022**, *144*, 16423–16432; b) Z. Mi, T. Zhou, W. Weng, J. Unruangsri, K. Hu, W. Yang, C. Wang, K. A. I. Zhang, J. Guo, *Angew. Chem. Int. Ed.* **2021**, *60*, 9642–9649; c) Z. Chen, J. Wang, M. Hao, Y. Xie, X. Liu, H. Yang, G. I. N. Waterhouse, X. Wang, S. Ma, *Nat. Commun.* **2023**, *14*, 1106; d) E. Jin, S. Fu, H. Hanayama, M. A. Addicoat, W. Wei, Q. Chen, R. Graf, K. Landfester, M. Bonn, K. A. I. Zhang, H. I. Wang, K. Mullen, A. Narita, *Angew. Chem. Int. Ed.* **2022**, *61*, e202114059; e) M. Lu, J. Liu, Q. Li, M. Zhang, M. Liu, J. L. Wang, D. Q. Yuan, Y. Q. Lan, *Angew. Chem. Int. Ed.* **2019**, *58*, 12392–12397.
[13] a) H. Wang, C. Yang, F. Chen, G. Zheng, Q. Han, *Angew. Chem. Int. Ed.* **2022**, *61*, e202202328; b) S. Ma, T. Deng, Z. Li, Z. Zhang, J. Jia, G. Wu, H. Xia, S. W. Yang, X. Liu, *Angew. Chem. Int. Ed.* **2022**, *61*, e202208919; c) S. Xu, M. Richter, X. Feng, *Acc. Mater. Res.* **2021**, *2*, 252–265; d) S. Yang, W. Hu, X. Zhang, P. He, B. Pattengale, C. Liu, M. Cendejas, I. Hermans, X. Zhang, J. Zhang, J. Huang, *J. Am. Chem. Soc.* **2018**, *140*, 14614–14618; e) R. Chen, Y. Wang, Y. Ma, A. Mal, X. Y. Gao, L. Gao, L. Qiao, X. B. Li, L. Z. Wu, C. Wang, *Nat. Commun.* **2021**, *12*, 1354.
[14] a) C. Li, J. Liu, H. Li, K. Wu, J. Wang, Q. Yang, *Nat. Commun.* **2022**, *13*, 2357; b) H. Ben, G. Yan, H. Liu, C. Ling, Y. Fan, X. Zhang, *Adv. Funct. Mater.* **2022**, *32*, 2104519.
[15] a) K. Gottschling, G. Savasci, H. Vignolo-Gonzalez, S. Schmidt, P. Mauker, T. Banerjee, P. Rovo, C. Ochsenfeld, B. V. Lotsch, *J. Am. Chem. Soc.* **2020**, *142*, 12146–12156; b) T. Banerjee, F. Haase, G. Savasci, K. Gottschling, C. Ochsenfeld, B. V. Lotsch, *J. Am. Chem. Soc.* **2017**, *139*, 16228–16234.
[16] W. Chen, L. Wang, D. Mo, F. He, Z. Wen, X. Wu, H. Xu, L. Chen, *Angew. Chem. Int. Ed.* **2020**, *59*, 16902–16909.
[17] S. Ghosh, A. Nakada, M. A. Springer, T. Kawaguchi, K. Suzuki, H. Kaji, I. Baburin, A. Kuc, T. Heine, H. Suzuki, R. Abe, S. Seki, *J. Am. Chem. Soc.* **2020**, *142*, 9752–9762.
[18] Y. Qian, D. Li, Y. Han, H. L. Jiang, *J. Am. Chem. Soc.* **2020**, *142*, 20763–20771.
[19] a) W. Li, X. Huang, T. Zeng, Y. A. Liu, W. Hu, H. Yang, Y. B. Zhang, K. Wen, *Angew. Chem. Int. Ed.* **2021**, *60*, 1869–1874; b) Y. Wang, W. Hao, H. Liu, R. Chen, Q. Pan, Z. Li, Y. Zhao, *Nat. Commun.* **2022**, *13*, 100; c) M. Hao, Y. Xie, X. Liu, Z. Chen, H. Yang, G. I. N. Waterhouse, S. Ma, X. Wang, *JACS Au* **2023**, *3*, 239–251; d) Y. Zhu, D. Zhu, Y. Chen, Q. Yan, C.-Y. Liu, K. Ling, Y. Liu, D. Lee, X. Wu, T. P. Senftle, R. Verduzco, *Chem. Sci.* **2021**, *12*, 16092–16099; e) M. Calik, F. Auras, L. M. Salonen, K. Bader, I. Grill, M. Handloser, D. D. Medina, M. Dogru, F. Lobermann, D. Trauner, A. Hartschuh, T. Bein, *J. Am. Chem. Soc.* **2014**, *136*, 17802–17807; f) Y. Song, A. Li, P. Li, L. He, D. Xu, F. Wu, F. Zhai, Y. Wu, K. Hu, S. Wang, M. V. Sheridan, *Chem. Mater.* **2022**, *34*, 2771–2778.
[20] R. Freund, S. Canossa, S. M. Cohen, W. Yan, H. Deng, V. Guillerm, M. Eddaoudi, D. G. Madden, D. Fairen-Jimenez, H. Lyu, L. K. Macreadie, Z. Ji, Y. Zhang, B. Wang, F. Haase, C. Woll, O. Zaremba, J. Andreo, S. Wuttke, C. S. Diercks, *Angew. Chem. Int. Ed.* **2021**, *60*, 23946–23974.
[21] a) X. Zhao, H. Pang, D. Huang, G. Liu, J. Hu, Y. Xiang, *Angew. Chem. Int. Ed.* **2022**, *61*, e202208833; b) X. R. Ren, B. Bai, Q. Zhang, Q. Hao, Y. Guo, L. J. Wan, D. Wang, *J. Am. Chem. Soc.* **2022**, *144*, 2488–2494; c) X. Li, C. Zhang, S. Cai, X. Lei, V. Altoe, F. Hong, J. J. Urban, J. Ciston, E. M. Chan, Y. Liu, *Nat. Commun.* **2018**, *9*, 2998.
[22] J. Feng, Y. J. Zhang, S. H. Ma, C. Yang, Z. P. Wang, S. Y. Ding, Y. Li, W. Wang, *J. Am. Chem. Soc.* **2022**, *144*, 6594–6603.
[23] C. Lu, P. Zhang, S. Jiang, X. Wu, S. Song, M. Zhu, Z. Lou, Z. Li, F. Liu, Y. Liu, Y. Wang, Z. Le, *Appl. Catal. B* **2017**, *200*, 378–385.
[24] a) H. Yang, X. Liu, M. Hao, Y. Xie, X. Wang, H. Tian, G. I. N. Waterhouse, P. E. Kruger, S. G. Telfer, S. Ma, *Adv. Mater.* **2021**, *33*, 2106621; b) X. Liu, Y. Xie, M. Hao, Z. Chen, H. Yang, G. I. N. Waterhouse, S. Ma, X. Wang, *Adv. Sci.* **2022**, *9*, 2201735.
[25] S. Chu, A. Majumdar, *Nature* **2012**, *488*, 294–303.
[26] S. Kushwaha, K. Patel, *Chem* **2021**, *7*, 271–274.
[27] a) M. Hao, Z. Chen, X. Liu, X. Liu, J. Zhang, H. Yang, G. I. N. Waterhouse, X. Wang, S. Ma, *CCS Chem.* **2022**, *4*, 2294–2307; b) Z. Wang, R. Ma, Q. Meng, Y. Yang, X. Ma, X. Ruan, Y. Yuan, G. Zhu, *J. Am. Chem. Soc.* **2021**, *143*, 14523–14529; c) W. R. Cui, F. F. Li, R. H. Xu, C. R. Zhang, X. R. Chen, R. H. Yan, R. P. Liang, J. D. Qiu, *Angew. Chem. Int. Ed.* **2020**, *59*, 17684–17690; d) T. Feng, Y. Yuan, S. Zhao, L. Feng, B. Yan, M. Cao, J. Zhang, W. Sun, K. Lin, N. Wang, *Angew. Chem. Int. Ed.* **2022**, *61*, e202115886.

Manuscript received: March 2, 2023
Accepted manuscript online: April 28, 2023
Version of record online: May 24, 2023